Developments in the Built Environment 23 (2025) 100709

Contents lists available at ScienceDirect

Developments in the Built Environment

journal homepage: www.sciencedirect.com/journal/developments-in-the-built-environment

Multi-scale X-ray techniques for assessing recycled concrete aggregate: from XRPD analysis of leftover cement in recycled aggregates to micro-CT imaging of concrete microstructure

A. Bisciotti [a,*], L. Mancini [b], A. Viani [c], V. Zalar Serjun [b], A. Mladenovic [b], G. Cruciani [a]

[a] University of Ferrara, Department of Physics and Earth Science, Via Saragat 1, 44122, Ferrara, Italy
[b] Slovenian National Building and Civil Engineering Institute - ZAG, Dimičeva ulica 12, 1000, Ljubljana, Slovenia
[c] University of Modena and Reggio Emilia, Department of Chemical and Geological Sciences, Via Campi 103, 41125, Modena, Italy

ARTICLE INFO

Keywords:
Recycled concrete aggregate
Leftover cement paste
CDW
X-ray diffraction
Microstructure

ABSTRACT

The content of leftover cement paste is a crucial parameter for determining recycled aggregates quality. Various methods assess this, including wet techniques (acid dissolution, chemical degradation, water absorption), physical approaches (freeze-thaw cycles, mechanical shredding, oven-dried density, thermal disaggregation), and spectroscopic or microscopy analyses. However, these methods often lack accuracy, are time-consuming, or depend on operator skill. A novel X-ray Powder Diffraction and Rietveld quantitative phase analysis approach is introduced to improve measurements precision. Results are compared with multi-scale analyses (microscopy, X-ray computed tomography, mechanical testing) on recycled aggregate concrete specimens. Findings highlight a strong correlation between leftover cement paste content and key concrete properties, including microstructure, hydration products, and mechanical performance. This study confirms that leftover cement paste content is a decisive factor in recycled concrete aggregate properties, and that the proposed method offers a rapid and reliable approach to control this parameter.

1. Introduction

Construction and demolition waste (CDW) is one of the main categories of waste produced globally, so its recycling within a circular economy to produce new building materials has become crucial (J. Li et al., 2023; Su et al., 2024). Recycled aggregates (RAs), which are produced from CDW, might reduce the total environmental impact of concrete production by reducing the mining of natural resources from aggregate quarries and pits (Dinh et al., 2022; Nilimaa, 2023). It is commonly acknowledged that RAs derived from the comminution of CDW are potential substitutes for natural aggregates (NAs) in construction projects (Althoey et al., 2023; Karlsson et al., 2021). At the same time, the current use of these secondary raw materials is mostly devoted to sub-bases and bases of pavements of roads and highways, where they are employed in unbound layers and low-grade concretes (C. Zhang et al., 2020). The limited adoption of RAs in high-grade applications (i.e., structural concrete) comes from the composite nature, and high heterogeneity of these secondary raw-materials, resulting in uneven interactions with cementitious binders (Djerbi, 2018). In fact, when directly produced from CDW crushed concrete, RAs are typically composed of the original NAs and of a variable amount of leftover cement paste (LCP) clinging to the surface (de Juan and Gutiérrez, 2009). The final properties of recycled aggregate concrete, where RAs are used instead of natural counterparts, are adversely impacted by the amount of LCP (Bai et al., 2020; J. Kim, 2022; Seo and Choi, 2014). This characteristic is considered as the primary obstacle that prevents the use of RAs in new structural high-grade concrete (Tam et al., 2021; Verian et al., 2018). Compared to natural rocks, the LCP increases the average porosity and reduces the bulk density of such aggregates, which is a major reason for the observed decline in fresh-mixing properties (Deng et al., 2023; Faleschini et al., 2014; B. Li et al., 2021), mechanical performances (Piccinali et al., 2022; B. Wang et al., 2021a), and durability of recycled aggregate concrete (Guo et al., 2018), affecting the confidence of the stakeholders in adopting RAs. The content of LCP within RAs is known to vary depending on the average RA diameter size, crushing methods, aging and original strength grade of the LCP, thus

This article is part of a special issue entitled: Novel Materials Testing published in Developments in the Built Environment.

* Corresponding author.
E-mail address: andrea.bisciotti@unife.it (A. Bisciotti).

https://doi.org/10.1016/j.dibe.2025.100709
Received 29 November 2024; Received in revised form 30 June 2025; Accepted 2 July 2025
Available online 11 July 2025

affecting the final properties of concrete with a variable and unpredictable order of magnitude (Chen et al., 2024).

The measure of the LCP content is crucial in determining the quality of RAs and shall become a mandatory step prior to the batching plant process. Despite this requirement, an internationally standardized procedure has not yet been established, whereas different methods have been proposed and are currently in use, as summarized in (Braymand et al., 2017; Tam et al., 2021). Existing protocols for measuring LCP content in RAs span a wide range of approaches. Among them, wet methods - such as acid dissolution, chemical degradation and water absorption - are the most commonly employed. They measure either a negative mass variation following the acid-induced dissolution of the LCP (Lal Chauhan and Jail Singh, 2023) or a positive mass variation due to retained fluids, as in the case of saturated-surface-dried water absorption tests (Duan et al., 2022). Alternatively, physical methods—including freeze-thaw cycles, mechanical shredding, oven-dried density, and thermal disaggregation—might also be employed to remove LCP and quantify its content (dos Santos Macedo et al., 2019; Zhao et al., 2013). In some cases, a combination of both approaches has been proposed and applied (Tam et al., 2021). A more advanced and precise strategy involves spectroscopic and microscopy techniques (Hu et al., 2024), often complemented by computer-based image analysis (Bisciotti et al., 2024; Y. Wang et al., 2021b). However, many of these procedures are time-consuming and not suitable for routine quality monitoring, while others fail to offer a clear and straightforward measure of this feature (Rangel et al., 2019). The wet acid methods, for example, may overestimate the cement paste content when recycled aggregates contain limestone, or many other acid-soluble rocks and minerals (Ulsen et al., 2022). Similarly, the absorption methods are influenced by the LCP porosity. Physical approaches are invasive, non-reproducible and their result typically depends on the original strength grade of the LCP (Martín-Morales et al., 2013). Microscope investigation is typically highly operator dependent. Whereas methods based on the chemical composition (e. g., X-ray fluorescence) are yet unable to distinguish LCP from limestone content (Angulo et al., 2009). In this scenario, X-ray Powder Diffraction (XRPD) may offer a valuable alternative solution. This method has grown beyond its roots in the world of laboratory research and is regarded as one of the most powerful industrial process-control tools in the field of building materials and minerals (Meier et al., 2012). XRPD opens enormous possibilities for *in-situ* monitoring of process and quality control, even in the field of continuous on-line measurements during industrial production (Dhanjal et al., 2006; Gugin et al., 2024). The use of XRPD to quantify LCP content in RAs has been previously explored (Bisciotti et al., 2024). The estimation is based on XRPD quantitative phase analysis by the Rietveld method (Aranda et al., 2012). The results reflect the crystalline assemblage in RAs, distinguishing rock forming minerals of the NAs from the LCP clinker and binder constituents. In terms of acquisition speed, the introduction of ultra-fast silicon-based linear and two-dimensional detectors has led to up to a 150-fold increase (Anderson et al., 2015). A scan that once required 3 h to collect data can now be completed in less than 2 min, with some advanced settings achieving results in just a few seconds (D. O'Flynn et al., 2013). The Rietveld approach, which is the bottleneck of the method proposed, can also be automated to speed up the methodology and reduce human mistakes using machine learning algorithms (Feng et al., 2019; H. Kim and Yoon, 2024). The whole process, from sample preparation to Rietveld calculations, can be completed in less than 30 min.

With the aim of testing the aforementioned method and validate the possible testing protocol, different samples from coarse, fine and ultrafine RAs are substituted to NAs in a fixed proportion into concrete. All the RAs samples were previously analyzed using XRPD and the Rietveld method, employing the results of the quantitative phase analysis to infer the LCP content. Afterward, a fixed mix-design formulation—where the cement type, water-to-cement ratio, and mixing and curing procedures are kept constant—is adopted for more accurate tracking of the microscopic features that emerge from RAs usage. The investigation of the concrete microstructure is conducted using lab-based X-ray computed tomography (X-ray micro-CT) in conjunction with optical microscopy (OM) and scanning electron microscopy (SEM). A detailed review of X-ray micro-CT application to cement and concrete materials can be found in da Silva (2018). This technique allows the microstructural characterization of a large range of materials in the three-dimensional (3D) domain with a non-destructive approach (Baker et al., 2012). Ultimately, quantitative data gathered from multi-scale analyses—including pore size, geometry, and connectivity—and concrete mechanical testing, are compared with LCP measurements obtained from the novel XRPD-based methodology.

2. Materials and methods

2.1. Natural and recycled aggregates

The NAs used are sand and gravel from the River Po (Italy), which are described based on UNI EN 932–3:2022. The gradation of the materials is shown in Fig. 1. The starting CDW contains more than 90 % of structural concrete (>40 MPa, 28 days compressional strength), the crushed concrete RAs are obtained from the demolition of a structure originally composed of white cement. The materials are collected from the stock piles in accordance with standard UNE-EN 932-1 (1998). After dry sieving (UNI EN 933-1, 2012), the obtained size distributions are used to replace NAs in the mix-design (Table 1) maintaining the final granulometric curve unaltered.

2.2. Concrete formulation

The mix-design of the concrete is done according to the British Department of the Environment (DOE) standard method (Teychenne et al., 1997), which targeted a compressive strength of 25 MPa on the 28th day. Type CEM I Portland cement 52.5 R is used, having a sharply different color from the residual white cement paste clinging to the RAs. River Po (Italy) sand and gravel are used as both fine and coarse NAs. Besides the reference concrete (named NAC) made only of NAs, there are notably three other types of mixtures prepared by replacing the NAs with three individual classes of RAs having different diameter sizes: 10 - 4 mm (CRA), 4–0.6 mm (FRA), and 0.6–0 mm (UFRA), although they come from the same original source. The replacement percentage of RAs is calculated based on the total weight of the aggregate content, entirely substituting the corresponding size fraction from the mix-design results. The mix-design for all the specimens is presented in Table 1. The water-binder ratio is kept at 0.58 in all the mixtures. No chemical admixtures are used.

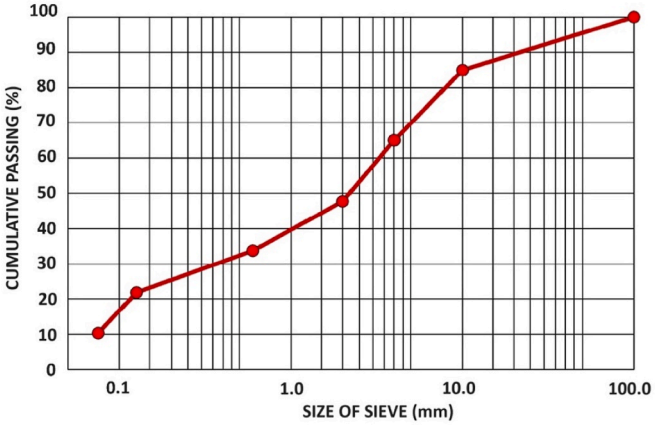

Fig. 1. Gradation curve of the natural aggregate.

Table 1
Material content within the concrete specimen according to the mix-design obtained with the British DOE Standard Method (Teychenne et al., 1997).

Material content (kg/m3)							
Mixture	Cement	NA	CRA	FRA	UFRA	Water	W/C
NAC	313.64	1822.68	–	–	–	181.68	0.58
CR104	313.64	1184.80	637.88	–	–	181.68	0.58
CR406	313.64	1251.51	–	571.17	–	181.68	0.58
CR060	313.64	1209.05	–	–	613.64	181.68	0.58

2.3. Testing protocol

The samples of RAs analyzed, divided into the aforementioned classes (CRA, FRA, UFRA), are obtained in the lab using a quartering method according to UNE-EN 932–2, 2000. Starting from each RA mound, 10 % of the material content is collected and shredded into fine powder using a jaw-crusher, followed by a mechanical press. The fine powders obtained are directly analyzed through XRPD. From the results employing Rietveld quantitative phase analysis, the wt. (%) of the different crystalline constituents of the RAs is used to obtain the LCP content according to the method proposed in Bisciotti et al. (2024). Subsequently, all the designed concrete mixtures have been produced according to UNI EN 206:2021. The specimens are cast in laboratory conditions and demolded 24 ± 2 h after mixing, then fully submerged in water at a temperature of 25 ± 2 °C until the age of testing. The determination of the flexural and compressive strength is done after 7, 28, and 90 days of curing. Following a first investigation with OM and SEM, the concrete samples are subjected to X-ray micro-CT analysis. Different microstructural characteristics of the concrete specimens are quantified from the 3D tomographic reconstruction and from further image analysis process. The obtained results are compared and discussed. Fig. 2 schematically depicts the testing protocol.

2.3.1. Recycled aggregates analyses and mineralogical model

Using a Bruker D8 Advance Da Vinci diffractometer at room temperature, XRPD patterns were collected in the 2 θ range of 5–90° at the Department of Physics and Earth Science of the University of Ferrara. The phase identification was carried out with DIFFRACT.EVA suite utilizing the Powder Diffraction File (PDF-2) database maintained by the International Centre for Diffraction Data (ICDD). An accurate quantitative phase analysis was then performed by the Rietveld profile fitting method applied to the X-ray diffraction patterns, using the Bruker TOPAS 5.0 software. The results provided a direct weighted (wt. %) quantification of the natural fragments dispersed in the RAs, the residual clinker minerals, the hydration phases, and of the carbonation products resulting from the latter. Four main classes of crystalline micro-constituents are defined for the RA materials as follows:

- Rock-forming minerals (RFM) related to the NAs original fraction (quartz, feldspars, chlorite etc.).
- Unreacted-cement (UC) for the anhydrous clinker phases (alite C_3S, belite C_2S, aluminate C_3A – calcium aluminoferrite C_4AF is not present here due to the white cement composition).
- Hydrated-cement (HC) for the hydration products (portlandite CH, ettringite AFt and AFm phases, namely the hydrated calcium aluminates based on the hydrocalumite-like structure). For the C-S-H gel component, a tobermorite-like structure was used (Mesecke et al., 2022), and a crystallite size of 1.5 nm was fixed to obtain a profile fitting that follows the amorphous content.
- Carbonated-cement (CC) for the calcite polymorphs (calcite, vaterite, aragonite).

During the Rietveld calculation, the individual peak shape functions of the crystalline constituents were summed and combined with a background function. The background was modeled using a three-term Chebyshev polynomial equation over the entire 2θ range to maintain an almost linear profile. This approach allowed for the visualization and quantification of the semi-amorphous C-S-H peak, which overlaps with the background and lies beneath the bases of the more crystalline peaks. The weight percentages (wt.%) of each crystalline phase were determined based on their peak positions and relative intensities. The goodness of fit was evaluated using the Residual Weighted Profile (Rwp) value and by visually assessing the difference between the observed and calculated profiles on the same scale.

2.3.2. Microstructural investigation of concrete

To undertake the microstructure examination, concrete sections embedded in epoxy resin from various specimens were observed using OM and SEM. The SEM device employed is a JEOL JSM-IT500 with an EDS detector and a BSE backscattered electron detector. The acquisitions were carried out in low-vacuum mode, allowing imaging and analysis of uncoated materials at a gun voltage of 15.0 kV. Concrete

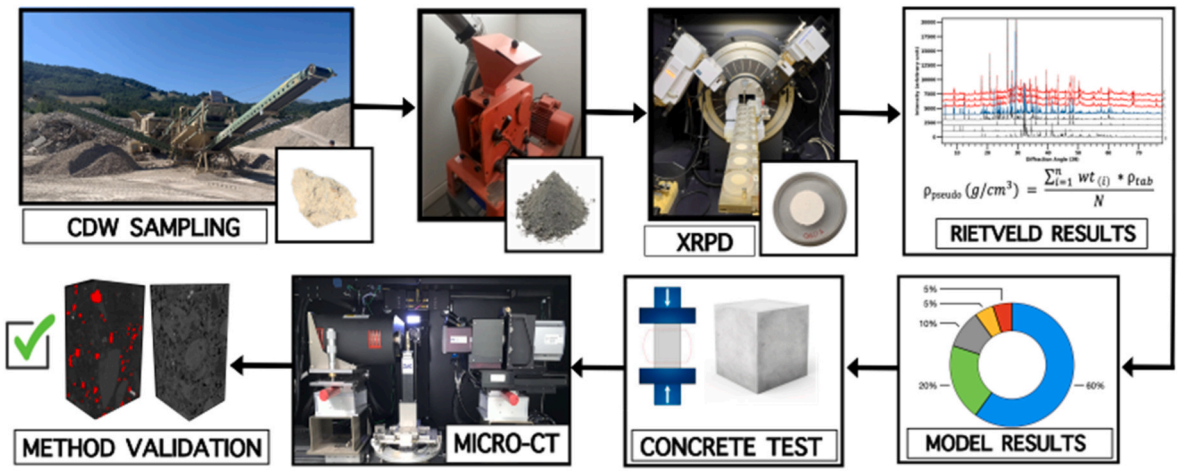

Fig. 2. Testing protocol for leftover cement paste monitoring and validation from the concrete microstructure.

specimens of 10x10 × 60 mm were cut and imaged using X-ray micro-CT. The micro-CT analyses were performed using a Zeiss XRadia's MicroXCT-400 instrument available at the Materials Department of ZAG (Slovenia) with the following operating parameters: voltage = 80 kV, source power = 10 W, LE2 filtering, source-to-sample distance = 52.5 mm, and source-to-detector distance = 150 mm. For each sample, a series of 1600 radiographs (projections) was acquired over a total angle of 360°, with an exposure time per projection of 3 s and an effective pixel size of 17.6 μm. The tomographic reconstruction was performed using the XRM Zeiss reconstruction software. This software also allows to apply a beam hardening correction to the images. The resulting reconstructed axial slices are in 16-bit TIFF format. The processing and analysis of the reconstructed 3D data was performed using the DragonFly software (version 2022.2, free license for academic users) by ORS (Canada). The quantitative parameters extracted from the volumetric images were selected with an emphasis on the pore system, including porosity (volume %), pore size distribution, pore spatial distribution and connectivity. After an optimization procedure, the following multi-stage protocol was adopted:

(1) For all imaged specimens, the original reconstructed slices were converted to 16-bit raw format, using the Fiji software (Schneider et al., 2012), in the same interval of gray level intensities in order to compare the gray level values assigned to pores (the darkest areas), silica mineral particles (the brightest areas), and the cement matrix (the areas with intermediate intensity).
(2) From the overall reconstructed volumes, the background areas were removed after defining a Volume of Interest (VOI) from the concrete specimens which is made out of cropped rectangular prisms. For each imaged specimen, a VOI composed of (365 x 390 x 830) voxels (corresponding to ca. 6.40 x 6.85 × 15 mm^3) was selected. The VOI must include all relevant morphological features of interest, such as the old and new cement matrix, pores, and D-ITZ, being at the same time a representative elementary volume (REV). Due to the inclusion of aggregate particles, concrete specimens usually have high pore volume variations and low connectivity within similar VOIs (Yio et al., 2017). Therefore, the REV assessment was undertaken by evaluating pores dispersion using the bounding box approach (Al-Raoush and Papadopoulos, 2010).
(3) The sample microstructure is composed of different phases of interest having broad compositional variability identified after the raw materials analysis (See Sec. 2.3.1). The main feature of interest is the porosity distribution. The 3D images were preprocessed with a grayscale-to-grayscale filter to reduce the noise and enhance its edges. A median filter wasafterwards appliedtogether with an unsharp filter to enhance the contrast and resolution of very fine pores. The resulting image was then segmented to obtain the binary distribution for the objects of interest. We adopted a semi-automated threshold-based segmentation process to optimally identify the pores by applying the 3D Otsu method (Otsu, 1979). The pores touching the edges of the ROI prism were excluded from the analysis in order to conduct a study only on the inner representative features. Quantitative analysis was carried out on this preprocessed image. For a meaningful description of the VOI, pores with volume less than 8 voxels were excluded from the quantitative analysis.
(4) After the segmentation procedure, it was possible to calculate the volume (%) of pores and to determine their spatial 3D distribution within the cement matrix as well as the main properties of interest such as geometrical features and connectivity. All this information was obtained after completing a skeletonization of the pore phase using the tool available in the Dragonfly software. This method allows extraction of the "spine" of a 3D object, generating a node at each pore location and node-to-node branches. Analyzing the skeleton morphology allows for a simpler 3D depiction of the pore network, providing quantitative data such as the number of nodes and the branch distribution (Zandomeneghi et al., 2010).
(5) Numerous statistical attributes were computed for each individual pore, in addition to their volume percentage (total porosity). These parameters were chosen after a review of the literature and variables found in studies on the porosity in bricks and other building materials. Among them, six parameters wereselected to characterize the microstructure of the investigated concrete samples, namely: pore volume, aspect ratio, sphericity and mean Feret diameter, as well as skeleton Euclidean length, and number of skeleton branches.

3. Results

3.1. X-ray powder diffraction and rietveld refinement

The XRPD pattern collected from the CRA, FRA and UFRA samples provides a unique 'fingerprint' information on the crystalline constituents from the bulk RAs assemblage. The Rwp values are displayed together with the measured and calculated profiles (Fig. 3). The results of the quantitative phase analysis applied to the X-ray diffraction patterns of the RAs are shown in Table 2.

From the peak positions, the occurrence of residual cement minerals (C_3S, C_2S, C_3A) and other secondary crystalline phases, which represent the hydration and carbonation products of the LCP, was identified. The C_3S phase used is the monoclinic form (M3), based on the CIF file determined in De La Torre et al. (2002). The C_2S employed is in the *alpha* form, which has a hexagonal structure (Mumme et al., 1995). C_3A is instead in the cubic space group, according to de Andrade Gobbo et al. (2004). The profile shape for the C-S-H semi-amorphous phase comes from the CIF file of 14 Å tobermorite, a crystalline natural analogue of C-S-H (Grangeon et al., 2013). By imposing a crystallite size below 5 nm, the C-S-H semi-amorphous structure was modeled (Duque-Redondo et al., 2022; Mesecke et al., 2022). Besides AFt (ettringite), two main AFm phases are identified, namely (1) and (2), respectively the hemi-carbo aluminate form and the mono-carbo aluminate one (Renaudin et al., 1999). The minerals accounting for RFM are mainly silicates and carbonates. Hence, the occurrence of feldspars, quartz, dolomite, iron-minerals (hematite and goethite) likely pertains to the original NA counterpart fragments. Hornblende, as well, is a common mineral often associated with volcanic and metamorphic rocks. Other phyllosilicate minerals (muscovite and chlorite) could mainly result from the fine NAs originally used or occasionally from soil mixing during disposal of CDW. Calcite is therefore present either as an aggregate (primary) or, more importantly, as a main carbonation product (secondary), together with vaterite and aragonite. Both primary (type-1) and secondary (type-2) calcite are revealed by the shape of main peak at 29.6° 2θ. The coexistence of two calcite types was modeled using two structures having different crystallite sizes: a type-1 calcite with an average crystallite size above 80 nm and a type-2 calcite with a value of 25–35 nm.

3.2. Mineralogical model

The results of the XRPD Rietveld quantitative phase analysis were used to obtain the volume of RFM, UC, HC, and CC for the different RAs used. The partial steps of calculation and relative volumes can be found in Table II of the Supplementary Materials. The results (Fig. 4) show that CRA have a higher volume fraction of RFM (%) related to the NAs counterpart (73 %), whereas for the FRA and UFRA, the values are progressively decrease (respectively 61 and 41 %). The opposite trend is found for the HC (%) volumes, which account for 25 % in the CRA, 37.5 % in FRA and 50 % in UFRA. A similar trend is observed for the UC%. The CC (%) is eventually very similar acrossall the different samples, accounting for only a few percentage points. In conclusion, from the sum

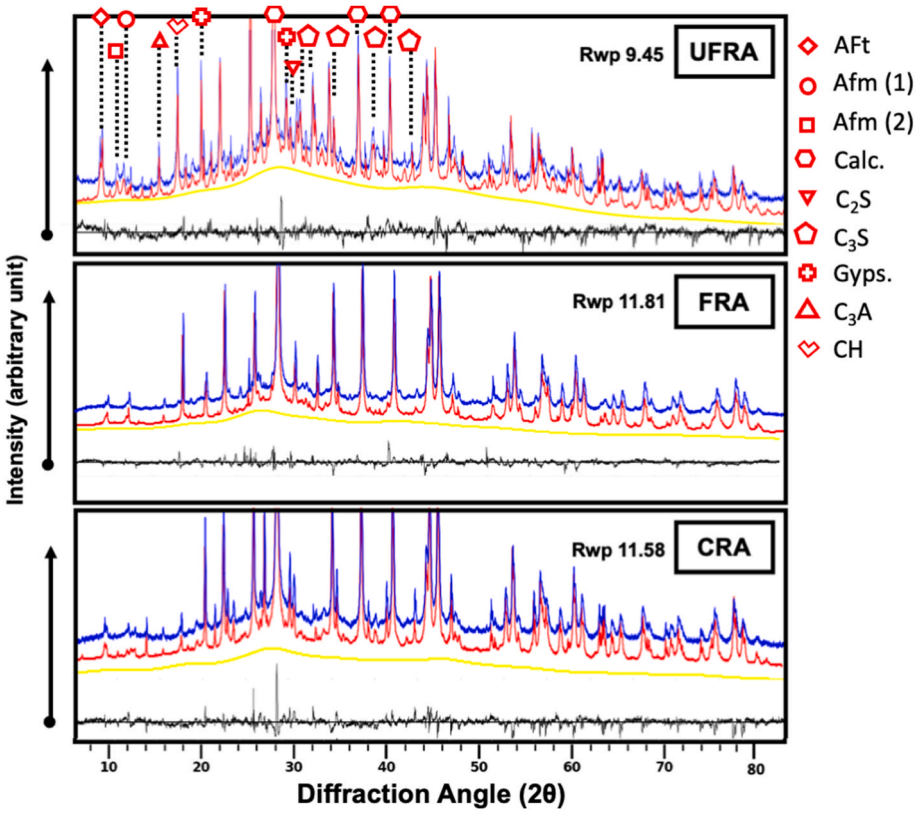

Fig. 3. XRPD diffraction patterns for the ultra-fine recycled aggregates (UFRA), fine recycled aggregates (FRA), and coarse recycled aggregates (CRA). The blue profile is the measured pattern, the red profile is the Rietveld calculation, the yellow is the C-S-H semi-amorphous profile and the black one the residual profile. The main peaks of the UC, HC and CC phases are shown. For the abbreviations, refer to Table 2.

Table 2
Rietveld quantitative phase analysis of the studied RA samples (UFRA, FRA, CRA) with the wt.% of mineral phases identified and classified as unreacted cement (UC), hydrated cement (HC), carbonated cement (CC), and rock forming minerals (R).

Mineral phases	Groups	UFRA	FRA	CRA
Calcite type-1	RFM	23.91	53.08	55.16
Quartz	RFM	7.14	3.54	9.29
Albite	RFM	0.96	0.00	1.88
Orthoclase	RFM	0.94	1.52	1.37
Chlorite	RFM	–	0.43	0.39
Muscovite	RFM	2.80	1.27	2.16
Dolomite	RFM	3.61	1.13	2.28
Lizardite	RFM	0.12	0.00	0.02
Goethite	RFM	0.18	0.04	0.03
Hematite	RFM	0.17	0.1	0.02
Horneblende	RFM	0.00	0.2	0.34
Kaolinite	RFM	1.35	0.00	0.45
Tricalcium Silicate (C_3S)	UC	3.74	0.23	0.19
Dicalcium Silicate (C_2S)	UC	2.21	0.52	0.60
Gypsum (Gyps.)	UC	0.13	0.40	0.36
C_3A	UC	0.15	0.04	0.05
C-S-H	HC	43.31	34.92	24.35
Ettringite (AFt)	HC	2.27	0.54	0.18
AFm (1)	HC	1.35	0.61	0.63
AFm (2)	HC	0.24	0.00	0.03
Portlandite (CH)	HC	1.95	0.84	0.20
Calcite type-2 (Calc.)	CC	3.06	0.40	0.00
Vaterite	CC	0.41	0.21	0.02

of the mentioned components, excluding the RFM (%) content, it is possible to assess the total LCP (%) content, which is found to be 59 % in UFRA, 39 % in FRA and 27 % in CRA.

3.3. Concrete microstructure analysis

The properties of the concrete samples, such as the cement matrix, aggregates, and ITZ surroundings, were also captured and outlined using OM. The new cement paste is gray, while the old LCP is composed of white cement, making it easy to distinguish between RAs and NAs. The reference concrete sample NAC is characterized by irregularly shaped NA grains with varying sizes well graded and evenly distributed (Fig. 5a). Quartz, feldspar, and rock fragments (e.g., granite, basalt, limestone) are common and have a spherical geometry, being river sediments. The petrography of sand and gravel from the Po' river, based on OM analysis, is provided in Table I of the Supplementary Materials. The cement paste matrix has a fine texture, forming an interwoven and homogenous mix with no local segregation (Fig. 5b). In sample RC104, multiple CRA particles can be seen and the LCP distribution appears uneven, where some grains are fully covered while others are only partially surrounded (Fig. 5c). This condition is a direct consequence of the crushing process of the original concrete-CDW source. (Chen et al., 2024). The variable LCP distribution results in the developing of ITZ (Fig. 5d). The concrete matrix seems gap-graded, with CRA particles generally larger than the corresponding NAs (within the same 10-4 mm size). However, the overall texture and mix remains comparable to the reference NAC.

The same cannot be said for RC406, which differs from the refence concrete. The ITZ layers formed after the introduction of FRA extend into a void area (Fig. 6e), showing a greater impact of LCP on a larger scale. Although the mix homogeneity and the aggregate gradation remains adequate, the matrix is less coherent, and local segregation, micro-cracks, and voids can be observed in the surroundings of the RAs (Fig. 6f). An even greater impact is observed in RC060, where the presence of UFRA significantly alters the cement texture and color, giving it a more brownish hue. (Fig. 6g). This is likely a consequence of

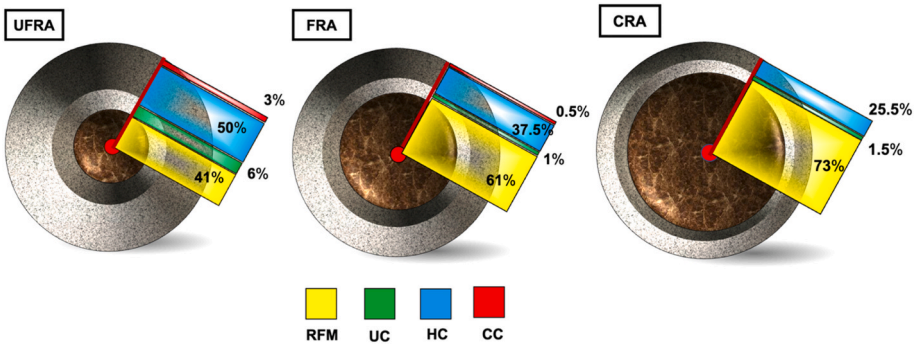

Fig. 4. Pie charts of the volume reconstructions according to the XRPD mineralogical model.

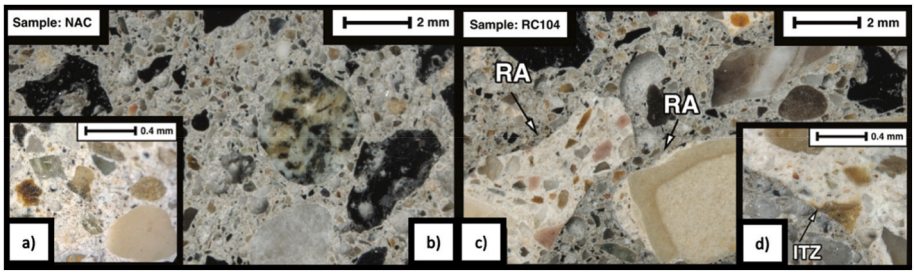

Fig. 5. Optical microscopy images of NAC and RC104 concrete specimen sections.

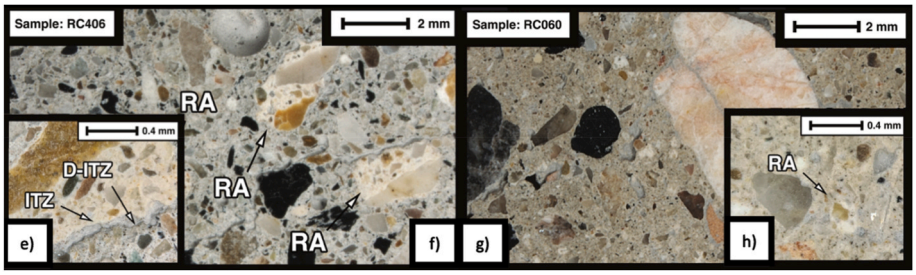

Fig. 6. Optical microscopy images of RC406 and RC060 concrete specimen sections.

higher content of fine clays and other soil minerals, as also indicated by the XRPD analysis (Table 2). The matrix is also gap-graded, and local segregation is common. Although RAs are not visible, high-magnification observation reveals that the LCP structure, and therefore of ITZ, is preserved even in the finest grains. (Fig. 6h).

The SEM investigation of concrete specimens provides both important morphological information and semi-quantitative chemical point analyses using the EDS detector. From the chemical perspective, the LCP composition closely resembles that of the fresh cement paste (Table III of Supplementary Materials). LCP exhibits higher calcium (CaO, 58–63 %) and lower silica content (SiO_2, 25–28 %) compared to the fresh cement paste, which has an inverse trend, with SiO_2 (45–50 %) and (CaO 29–34 %). These differences mainly arise from the superior carbonation degree of the LCP, which has also altered the morphology of the RAs (Fig. 7a). Another distinguishing feature is the slightly higher iron and alumina content in the fresh cement paste, which reflects the presence of clinker minerals like C_3A and C_4AF. Due to their comparable calcium-silicate nature, the D-ITZ is the main distinct feature indicating the presence of RAs (Fig. 7b). Indeed, the D-ITZ appears as an outer, lighter rim with voids and deformation zones within the new cement paste. It was

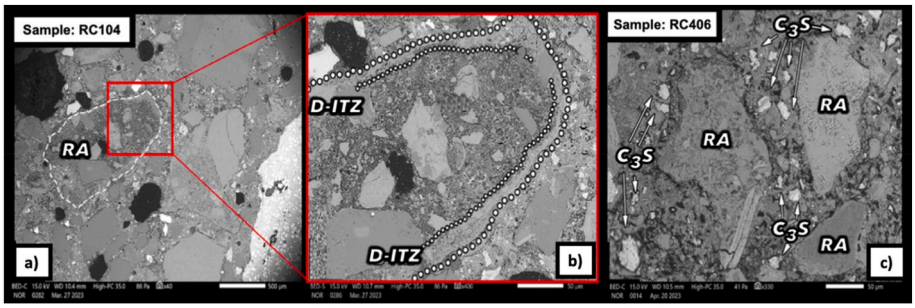

Fig. 7. SEM images of studied samples and BSE chemical semi-quantitative results from the point analyses.

possible to measure the D-ITZ average thickness, which, in agreement with previous literature, is found to be around 20 μm, although with considerable variations depending on the LCP content (Le and Bui, 2020; R. Wang et al., 2020). In the new cement paste of recycled concrete aggregate, following the BSE/EDS point analyses, the widespread presence of unreacted cement grains (e.g., C_3S - characterized by a well-preserved rectangular morphology) has been observed, particularly prominent in the proximity of RAs (Fig. 7c).

3.4. X-ray computed microtomography results

Based on the reconstruction of the micro-CT images (Fig. 8), a sequence of image processing operations was performed to quantify the sample's main features of interest (See Sec. 2.3.2).

The characteristic diameter of the RAs utilized (CRA, FRA and UFRA) is found to have a direct influence on shaping the porosity developed inside the cement matrix (Fig. 9). Both total porosity (%) and pore volume (mm^3), which is a measure of the average volume for the whole porosity distribution, decline linearly when RAs of smaller size are replaced in the reference mix-design (Table 3).

For the porous phase, diameters, volumes, surface areas, and sphericities of pores have been obtained, along with color-coded visualizations according to pore attributes. Numerous statistical attributes were computed for each individual pore, as shown in Table 3, in addition to their volume percentage (total porosity). The geometry of pores changes with the use of different RAs; the aspect ratio is higher for the RC060 (0.70) and steadily decreases until it reaches the NAC reference sample (0.64). The sphericity of the pores, which indicates the general geometry, exhibits the maximum value (0.94) in the NAC sample before steadily declining to the RC060 (0.91). The mean Feret diameter, which yields a mean value of the pore's diameter, shows that from the RC060 (0.06 mm) to the NAC sample (0.11 mm), the value doubles.

Furthermore, the score plot of the entire data distribution for the pores' volume displays some other interesting features (Fig. 10). While the NAC reference concrete has a conventional porosity distribution, with the prevalence of pores larger than 0.5 mm^3, all the other concrete specimens containing RAs exhibit a somewhat opposite trend. In these samples, finer pores with a maximum volume of 0.005 mm^3 prevail, which are not found in the reference concrete. It is worth mentioning the trend involving the fraction of the smallest pores within the recycled concrete itself (p. < 0.005 mm^3), whose contribution linearly increases with the inclusion of smaller-sized RA, from CR104 (around 350 counts) to CR060 (around 450 counts).

Another significant piece of information obtained from the micro-CT analysis involves the evaluation of the skeleton Euclidean length values and connectivity density (Table 3), which characterize the extension and number of possible paths that connect node-to-node and node-to-end branches, measured from a dense graph of the individual pores. From the skeleton Euclidean length (mm), the maximum distance in the porosity network is found in the reference natural aggregates concrete (NAC), with this value gradually decreasing with the introduction of smaller-diameter RAs. The count of skeleton branches, with lengths between 0 and 0.2 mm, displays even broader differences. RC060 has more than 80,000 local pores connections (Fig. 11). Comparing the other samples, we observe that the order of magnitude is roughly 10 times higher. In this regard, it is also interesting to point out that sample RC104 has less pore skeleton branches than the reference sample NAC.

3.5. Mechanical testing

The mechanical test results for the analyzed concrete specimens show a non-uniform pattern that explains the positive or negative impact of replacing NA with RAs in regular mix-design. As prior work has already shown (B. Wang et al., 2021a), there are significant variations between coarse (4–10 mm in size) and fine (below 4 mm in size) RAs utilization. Following 28 days of curing, the use of fine RAs, as observed for samples RC060 and RC406, led to a decrease of 38 % and 27 %, respectively, in comparison to the reference concrete's mechanical strength. In contrast, the use of coarse RAs, as in sample RC104, allowed to achieve a mechanical strength 7 % higher than of the reference NAC sample (Fig. 12). The observed reduction of mechanical properties at 90 days of curing for recycled aggregate concrete samples can be due to the aggregate-cement paste weakening caused by moisture absorption from the LCP that affects the bond strength, as reported previously (Etxeberria et al., 2007; Poon et al., 2004). This condition represents a substantial threat for the durability and safety of constructions that encompass RAs (J.C. Liu et al., 2023).

4. Discussion

4.1. Raw materials analyses and mineralogical model

The adoption of the XRPD method for characterizing RAs provides a rapid (less than 30 min) and precise approach for achieving a comprehensive volumetric reconstruction of the key features of these secondary raw materials (Fig. 4). Compared to other available testing methods for RAs, XRPD offers several advantages, particularly in assessing the LCP content. Beyond its fast acquisition time, this method also demonstrates superior reliability. Moreover, as noted in Section 3.3, RAs show considerable sample variability, with certain grains differing significantly from the rest. Since XRPD analyzes bulk samples, it delivers a more representative description compared to microscopy and SEM investigations, which may be less accurate depending on the focus of the observation and on the operator's expertise. Physical methods—such as freeze-thaw cycles, mechanical shredding, oven-dried density, and thermal disaggregation—are highly dependent on the properties of LCP

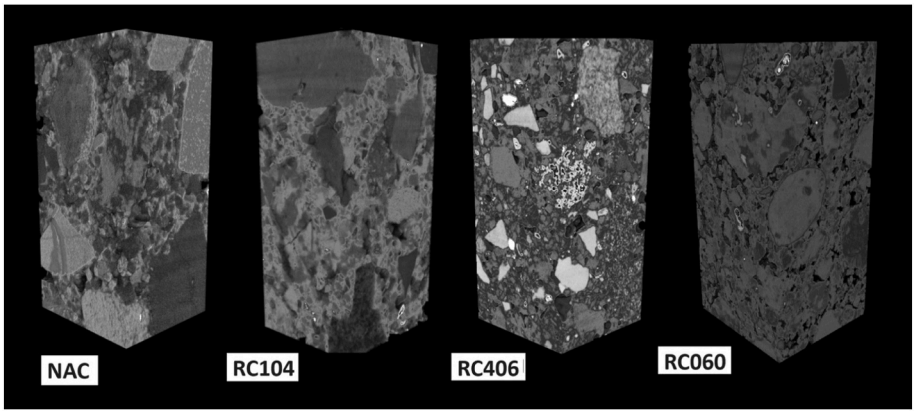

Fig. 8. 3D rendering of the investigated volume of interest (10 x 10 x 60) mm for different concrete specimens.

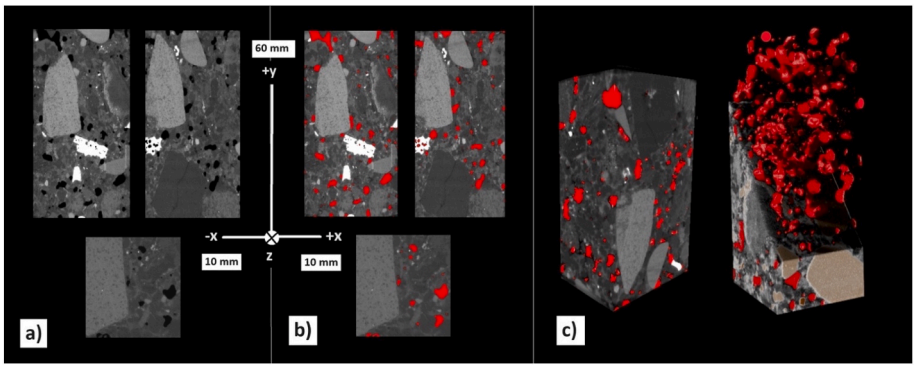

Fig. 9. Results of image processing and analysis for the reference sample NAC. a) Reconstructed slices in the main axial directions, b) the same slices after processing and segmentation, c) 3D total porosity distribution.

Table 3
Mean values of the variables obtained from the multi-ROI analysis used to describe the pore distribution for the different samples.

Samples	Total porosity (%)	Pores volume (mm^3)	Pores aspect ratio	Pores sphericity	Mean Feret diameter (mm)	Skeleton Euclidean Length (mm)	Connected skeleton branches count
NAC	5.4	0.008	0.64	0.94	0.11	0.18	6918
RC104	5.6	0.007	0.66	0.93	0.11	0.18	5989
RC406	6.7	0.004	0.66	0.93	0.10	0.17	8225
RC060	7.8	0.002	0.70	0.91	0.06	0.11	80640

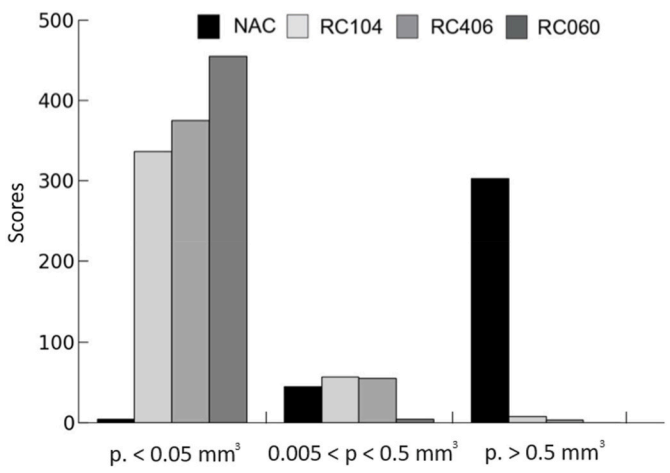

Fig. 10. Bar charts plot of the pore (p) volume (mm^3) distribution within the studied samples.

(Pepe et al., 2014). Significant variations in the adhesion strength of the LCP arise due to differences in the original cement type, water-to-cement ratio, aging conditions, carbonation degree, and other factors. Consequently, applying the same protocol can lead to inconsistent outcomes, compromising the reproducibility of the method. In contrast, the XRPD-based method proposed here identifies crystalline products associated with the LCP component based on their diffraction peak positions, which serve as unique fingerprints. These fingerprints are then translated into weighted volume information using the Rietveld method (Le Saoût et al., 2011). The accuracy of the results can also be monitored and assessed through the Rwp values, which quantify the difference between the reconstructed and measured XRPD profiles (Fig. 3). Eventually, RAs can be classified from high-quality to low-quality materials based on the ratio between RFM and LCP content. Indeed, the RFM value represents the volumetric reconstruction for the group of minerals attributed to the original aggregate embedded in the RAs. These fragments, mainly composed of silicate minerals, are primarily responsible for the positive contribution to the final mechanical performance of concrete. The anhydrous cement phases (UC) are clinker minerals that have not fully reacted during the hydration process, this is a normal and well-documented condition affecting cement pastes (Jansen et al., 2018). Identifying the UC minerals from XRPD is a basic task, and multiple papers document and explain the procedure (Aranda et al., 2012). More challenging are the measurements of HC and CC, which also contribute to the overall content of LCP. The C-S-H gel is the major product of the cement hydration process (Nonat, 2004), due to its poorly crystalline nature it is typically included in the XRD amorphous fraction, which can also be measured using different XRPD approaches ranging from the use of an internal standard to more complex ones (H. Kim and Yoon, 2024; X. Li and Scrivener, 2025). In the present research, with the aim of speeding up the procedure, the C-S-H has been measured through the Rietveld procedure by modeling a tobermorite-like structure with a small crystal size (below 5 nm). A more precise approach could result from the use of an internal standard, which, on the contrary, would increase the time needed. The method has been previously tested and described (Mesecke et al., 2022). Additionally, the Rietveld approach is also used to model the bi-modal crystallite size distribution of calcite. When analyzing concrete containing both limestone aggregates and carbonated cement paste using XRPD, the primary calcite peak at 29.6° 2θ often appears asymmetric. As discussed in Section 3.1, this asymmetry arises from the presence of two distinct calcite phases. The secondary calcite resulting from the carbonation of the LCP has a smaller crystalline site, and therefore can be distinguished from the primary one coming from the limestone content (Bisciotti et al., 2024). In conclusion, within the studied RAs it is found that the content of LCP increases exponentially with the decrease in the diameter. In agreement with most previous literature data (de Juan and Gutiérrez, 2009; Mazhoud et al., 2022).

4.2. Concrete microstructure investigation

The microstructure examination conducted through OM and SEM (Sec. 3.3) allowed the observation of the main macroscopical and microscopical features of the NAs and RAs and their relative impact on the concrete matrix. A primary difference between the two lies in the shape, geometry, and volume of the aggregates, in these aspects, RAs differs from NAs being largely influenced by the LCP content. This

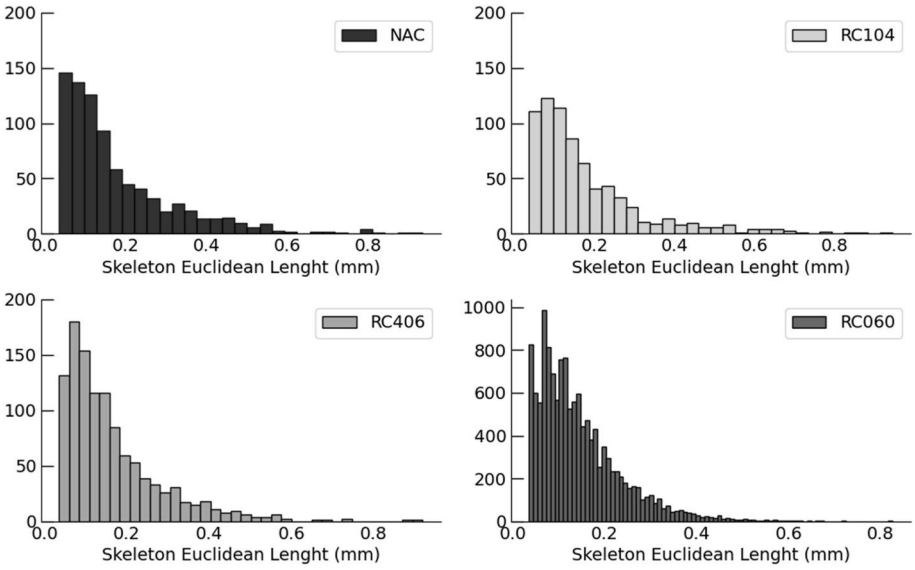

Fig. 11. Skeleton Euclidean length (mm) bar charts for the different specimens.

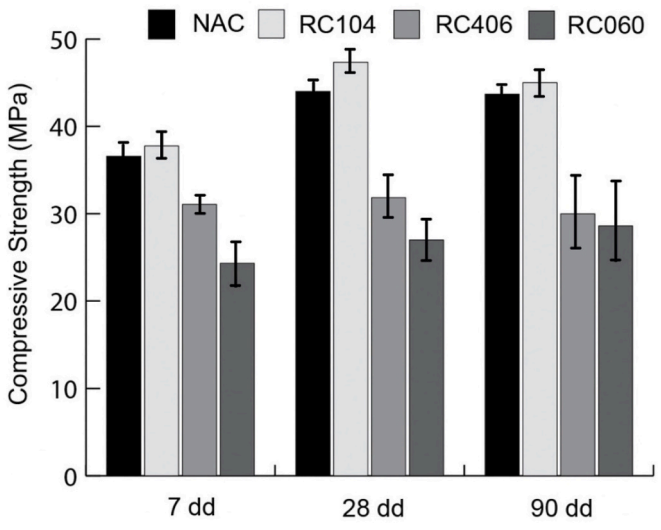

Fig. 12. Bar chart of the compressive strength after 7, 28 and 90 dd of curing.

variation directly impacts gradation and grain size distribution, ultimately affecting the concrete's final properties (Q. Liu et al., 2024; Ren et al., 2024). While CRA does not appear to significantly alter the concrete mix compared to the reference sample, FRA and UFRA introduce major secondary effects, such as local segregation, alteration of cement texture, and the formation of porosity and voids associated with the D-ITZ. The D-ITZ, also known as ITZ_4 - new mortar-bonded mortar (Lu et al., 2024), mainly represents void areas within the concrete matrix. Its development results from the local absorption and subsequent release of water from the LCP, affecting the hydration degree of the fresh cement around it (Erdem et al., 2018; Vargas et al., 2017). Clear evidence of this process is the presence of unreacted clinker minerals in the proximity of RAs, observed by SEM analyses, which indicates that the latter interacted with the fresh cement paste, absorbing part of the mixed water, locally hindering the process of hydration. This effect has shown a higher magnitude in the presence of UFRA, indicating higher absorption from the LCP. Again, following SEM imaging, the thickness of the D-ITZ layers was found to be in the range of 20–100 μm, as already described in previous literature (Fang et al., 2023), based on this evidence, the pixel size resolution for the micro-CT analysis was set below this value. As shown by the SEM-EDS chemical analysis, the main difference between LCP and fresh cement paste mainly lies in the carbonation degree. Therefore, this feature may represent a key parameter in controlling the interaction between RAs and new concrete, as observed in previous studies (J. Zhang et al., 2015).

Following the Micro-CT investigation, the total porosity inside the different concrete specimens was found to soar with the substitution of RAs, and with the reduction of the RAs' mean diameter (see total porosity (%) in Table 3). In detail, all of the RC specimens developed capillary porosity (volume size <0.05 mm^3), which is less abundant in the reference NAC sample (Fig. 13). Taking into account the size of the pores, using the mean Feret diameter (Table 3), the average radius of the pores is almost two times higher in the NAC sample (0.11 mm) compared to the RC specimens (0.06 mm). The number of small pores increases as the size of RAs decreases, peaking in the RC060 sample and diminishing through the RC406 and RC104 specimens.

The geometry of the pores described by their aspect ratio and sphericity values (Table 3) indicates that the use of finer RAs leads to the formation of more equidimensional pores (similar max/min axis) even if they are less spherical. Larger pores, albeit less uniform, are primarily found in NAC and are caused by entrapped air voids, which range in size from 50 to 300 μm, created during compaction and mixing stages. On the other hand, in the presence of RAs, widespread capillary pores are formed, which are more uniform and usually range in size from 10 nm to 10 μm. These pores develop when the fresh cement paste and the LCP interact (Sáez del Bosque et al., 2017; Zhan et al., 2020). Afterward, the pore skeletonization evidenced a correlation between the formation of a tight network of capillary pores and the decrease in the RAs' diameters. The information from the skeleton Euclidean length (mm) represents another key description of the pore distribution in the cement matrix. The use of small-diameter RAs causes the length of local-scale connections within the pores to decrease, as shown by the color visualization (Fig. 14). Eventually, with adoption and subsequent reduction of RAs size, the capillary pores formed are smaller, more frequent, and widespread, resulting in an increase in pore density connectivity (Table 3). This latter circumstance has a large impact on the overall microstructure of the concrete, representing diffused voids and unbound areas formed in the surroundings of RAs, specifically in the proximity of leftover cement paste. It is therefore possible to conclude that the described capillary porosity is effectively part of the D-ITZ layers.

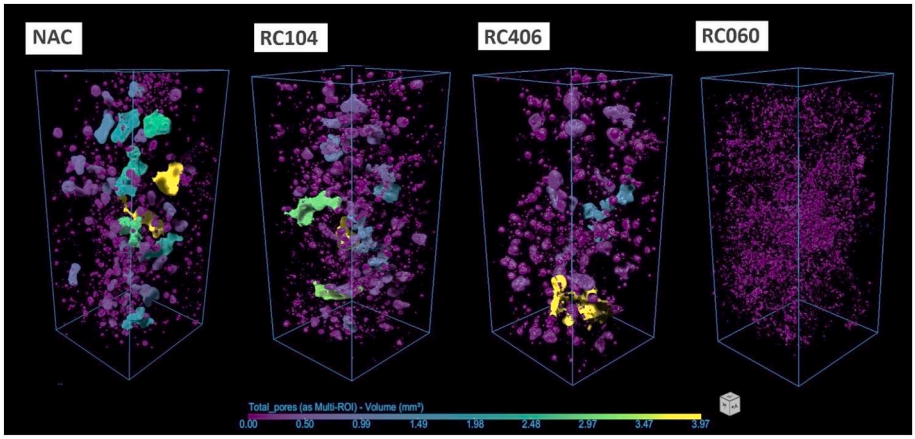

Fig. 13. 3D rendering showing the pores size distribution (color-coded) within the studied samples resulting from X-ray micro-CT data.

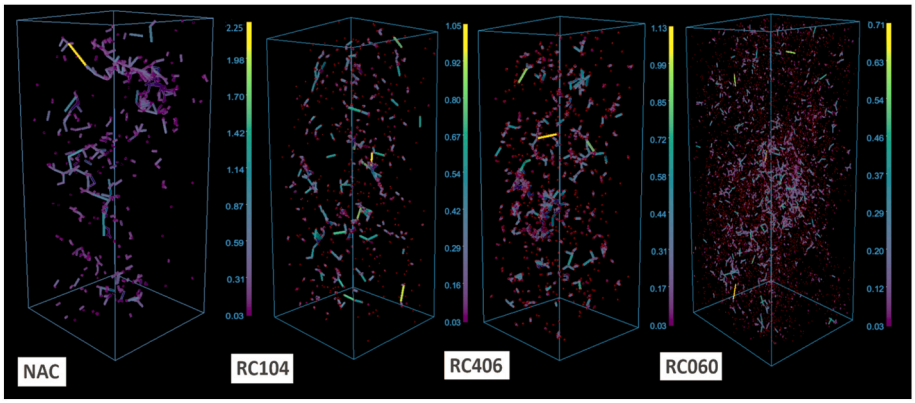

Fig. 14. Skeleton data with the color visualization of Euclidean length (mm) for the studied samples.

4.3. From the mineralogical model to the concrete properties

The importance of monitoring RAs quality, particularly in terms of LCP content, has been highlighted by the resultant impact on concrete microstructure and mechanical properties. For the studied samples, the content of LCP, as previously described, increases linearly with the decrease in the RAs' diameters 27 % in CRA, 39 % in FRA and 59 % in UFRA, in agreement with previous studies (Florea and Brouwers, 2013). These data, obtained from the XRPD analyses, are eventually compared with the information on the concrete microstructure obtained from the Micro-CT investigation. The number, volume, geometry, and network of pores are directly shaped by the RAs usage and especially by the LCP content. As the latter increases from 0 % (NAC samples) to 59 % (RC060), the average pore volume decreases from 0.08 mm^3 to 0.002 mm^3, representing a 75 % reduction. Simultaneously, the aspect ratio and sphericity of the pores are also affected, albeit to a lesser extent. The most significant impact, however, appears to result from the skeletonization of the pore matrix. When UFRA replaces NAs, the number of connected pores surges from approximately 7000 to nearly 80,000—a tenfold increase. This finding is particularly critical for understanding the corresponding deterioration in the mechanical properties of concrete incorporating these fine fractions of RAs. As previously discussed, the development of this capillary-connected porosity reflects the formation of D-ITZ layers, where the microcracks are known to be preferentially generated under loading (Xiong et al., 2016). Eventually, the macroscopic characteristics of concrete, like the mechanical performance, are also affected by the types of pores and their distribution, and therefore also directly by the LCP content (Kumar Mehta and Monteiro, 2006).

5. Conclusions

Existing protocols for measuring LCP content in RAs span a wide range of approaches, although a great number of them might not be accurate, reproducible, or fast enough. At the same time, monitoring the LCP content appears to be a mandatory step in assessing the quality of RAs. The method adopted and discussed in the present work, based on XRPD and Rietveld refinement, represents a valid, accurate, and fast protocol for the precise determination of this feature. Future developments could explore the use of machine learning to automate the Rietveld protocol following XRPD measurements, minimizing human errors and standardizing the procedure. Besides LCP quantification, the same method, can be further adopted to quantify the ratio of NAs present (RFM%) to other unwanted mineral components in CDW (ceramic, tiles, gypsum etc.). Moreover, the ageing of the CDW can be tracked (based on CC%), together with the disposal conditions. Based on such information, treatment methods can be chosen to improve CDW properties and/or to determine the best operating conditions for recycling in new applications, which may differ from the production of RAs, such as carbon capture and storage, clinker production, or the production of supplementary cementitious materials.

CRediT authorship contribution statement

A. Bisciotti: Writing – original draft, Methodology, Investigation, Formal analysis, Data curation, Conceptualization. **L. Mancini:** Writing – original draft, Supervision, Methodology, Data curation, Conceptualization. **A. Viani:** Writing – review & editing, Supervision, Methodology, Investigation, Data curation. **V. Zalar Serjun:** Methodology,

Investigation. **A. Mladenovic:** Writing – review & editing, Supervision, Project administration, Conceptualization. **G. Cruciani:** Writing – review & editing, Supervision, Funding acquisition, Conceptualization.

Funding

The project was financial supported under the National Recovery and Resilience Plan (NRRP), Mission 4, Component 2, Investment 1.1, Call for tender No. 104 published on February 2, 2022 by the Italian Ministry of University and Research (MUR), funded by the European Union – NextGenerationEU – Project Title "Rubble-to-Resource (RUB2RES): Earth science knowledge for sorting and recycling Construction and Demolition Waste" – CUP F53D23002140006 - Grant Assignment Decree No. 965 adopted on June 30, 2023 by the Italian Ministry of Ministry of University and Research (MUR).

Declaration of competing interest

The authors declare that they have no known competing financial interests or personal relationships that could have appeared to influence the work reported in this paper.

Acknowledgments

The authors want to thank Mateja Štefančič from Slovenian National Building and Civil Engineering Institute for assisting with mechanical testing of the concrete samples. We would also like to thank Tereza Fantová from the University of Ostrava for proofreading the work. Lastly, also Primož Oprčkal and Alenka Mauko Pranjic are acknowledged for the fruitful debates and for encouraging the research.

Appendix A. Supplementary data

Supplementary data to this article can be found online at https://doi.org/10.1016/j.dibe.2025.100709.

Data availability

No data was used for the research described in the article.

References

Al-Raoush, R., Papadopoulos, A., 2010. Representative elementary volume analysis of porous media using X-ray computed tomography. Powder Technol. 200 (1–2), 69–77. https://doi.org/10.1016/j.powtec.2010.02.011.

Althoey, F., Ansari, W.S., Sufian, M., Deifalla, A.F., 2023. Advancements in low-carbon concrete as a construction material for the sustainable built environment. Develop. Built Environ. 16. https://doi.org/10.1016/j.dibe.2023.100284.

Anderson, J., Gobbo, L.d.A., Weeren, H. van, 2015. X-Ray diffraction: new eyes on the process. IEEE Trans. Ind. Appl. 51 (1), 20–27. https://doi.org/10.1109/TIA.2014.2350557.

Angulo, S.C., Ulsen, C., John, V.M., Kahn, H., Cincotto, M.A., 2009. Chemical-mineralogical characterization of C&D waste recycled aggregates from São Paulo, Brazil. Waste Manag. 29 (2), 721–730. https://doi.org/10.1016/j.wasman.2008.07.009.

Aranda, M.A.G., De La Torre, Á.G., León-Reina, L., 2012. Rietveld quantitative phase analysis of OPC clinkers, cements and hydration products. Rev. Mineral. Geochem. 74, 169–209. https://doi.org/10.2138/rmg.2012.74.5.

Bai, G., Zhu, C., Liu, C., Liu, B., 2020. An evaluation of the recycled aggregate characteristics and the recycled aggregate concrete mechanical properties. Constr. Build. Mater. 240. https://doi.org/10.1016/j.conbuildmat.2019.117978. Elsevier Ltd.

Baker, D.R., Mancini, L., Polacci, M., Higgins, M.D., Gualda, G.A.R., Hill, R.J., Rivers, M. L., 2012. An introduction to the application of X-ray microtomography to the three-dimensional study of igneous rocks. Lithos 148, 262–276. https://doi.org/10.1016/j.lithos.2012.06.008.

Bisciotti, A., Jiang, D., Song, Y., Cruciani, G., 2024. Estimating attached mortar paste on the surface of recycled aggregates based on deep learning and mineralogical models. Cleaner Mater. 11, 100215. https://doi.org/10.1016/j.clema.2023.100215.

Braymand, S., Roux, S., Fares, H., Déodonne, K., Feugeas, F., 2017. Separation and quantification of attached mortar in recycled concrete aggregates. Waste Biomass Valorization 8 (5), 1393–1407. https://doi.org/10.1007/s12649-016-9771-2.

Chen, Y., Zhan, B., Hong, L., Guo, B., bian, P., Wang, C., Hong, X., Yu, Q., 2024. A new perspective on the effect of residual paste content on the properties of recycled fine aggregates. J. Build. Eng. 94, 110070. https://doi.org/10.1016/j.jobe.2024.110070.

da Silva, I.B., 2018. X-ray computed microtomography technique applied for cementitious materials: a review. Micron 107, 1–8. https://doi.org/10.1016/j.micron.2018.01.006. Elsevier Ltd.

de Andrade Gobbo, L., Sant'Agostino, L.M., Garcez, L.R., 2004. C3A polymorphs related to industrial clinker alkalies content. Cement Concr. Res. 34, 657–664. https://api.semanticscholar.org/CorpusID:96327061.

de Juan, M.S., Gutiérrez, P.A., 2009. Study on the influence of attached mortar content on the properties of recycled concrete aggregate. Constr. Build. Mater. 23 (2), 872–877. https://doi.org/10.1016/j.conbuildmat.2008.04.012.

De La Torre, Á.G., Bruque, S., Campo, J., Aranda, M.A.G., 2002. The superstructure of C3S from synchrotron and neutron powder diffraction and its role in quantitative phase analyses. Cement Concr. Res. 32 (9), 1347–1356. https://doi.org/10.1016/S0008-8846(02)00796-2.

Deng, X., Li, J., Lu, Z., Zhang, J., Luo, K., Niu, Y., Hu, J., He, K., 2023. Rheological and early hydration of cementitious material containing recycled concrete powders collected from recycled aggregates. Constr. Build. Mater. 393. https://doi.org/10.1016/j.conbuildmat.2023.132108.

Dhanjal, S.K., Young, L., Storer, P., 2006. Automatic control of cement quality using on-line XRD. IEEE Cement Industry Technical Conference, 2006. Conference Record, p. 17. https://doi.org/10.1109/CITCON.2006.1635726.

Dinh, H.L., Liu, J., Ong, D.E.L., Doh, J.H., 2022. A sustainable solution to excessive river sand mining by utilizing by-products in concrete manufacturing: a state-of-the-art review. Cleaner Mater. 6, 100140. https://doi.org/10.1016/j.clema.2022.100140.

Djerbi, A., 2018. Effect of recycled coarse aggregate on the new interfacial transition zone concrete. Constr. Build. Mater. 190, 1023–1033. https://doi.org/10.1016/j.conbuildmat.2018.09.180.

dos Santos Macedo, R., Ulsen, C., Mueller, A., 2019. Quantification of residual cement paste on recycled concrete aggregates containing limestone by selective dissolution. Constr. Build. Mater. 229. https://doi.org/10.1016/j.conbuildmat.2019.116875.

Duan, Z., Zhao, W., Ye, T., Zhang, Y., Zhang, C., 2022. Measurement of water absorption of recycled aggregate. Materials 15 (Issue 15). https://doi.org/10.3390/ma15155141. MDPI.

Duque-Redondo, E., Bonnaud, P.A., Manzano, H., 2022. A comprehensive review of C-S-H empirical and computational models, their applications, and practical aspects. In: Cement and Concrete Research, vol. 156. Elsevier Ltd. https://doi.org/10.1016/j.cemconres.2022.106784.

Erdem, S., Gürbüz, E., Uysal, M., 2018. Micro-mechanical analysis and X-ray computed tomography quantification of damage in concrete with industrial by-products and construction waste. J. Clean. Prod. 189, 933–940. https://doi.org/10.1016/j.jclepro.2018.04.089.

Etxeberria, M., Vázquez, E., Marí, A., Barra, M., 2007. Influence of amount of recycled coarse aggregates and production process on properties of recycled aggregate concrete. Cement Concr. Res. 37 (5), 735–742. https://doi.org/10.1016/j.cemconres.2007.02.002.

Faleschini, F., Jiménez, C., Barra, M., Aponte, D., Vázquez, E., Pellegrino, C., 2014. Rheology of fresh concretes with recycled aggregates. Constr. Build. Mater. 73, 407–416. https://doi.org/10.1016/j.conbuildmat.2014.09.068.

Fang, G., Chen, J., Dong, B., Liu, B., 2023. Microstructure and micromechanical properties of interfacial transition zone in green recycled aggregate concrete. J. Build. Eng. 66. https://doi.org/10.1016/j.jobe.2023.105860.

Feng, Z., Hou, Q., Zheng, Y., Ren, W., Ge, J.Y., Li, T., Cheng, C., Lu, W., Cao, S., Zhang, J., Zhang, T., 2019. Method of artificial intelligence algorithm to improve the automation level of rietveld refinement. Comput. Mater. Sci. 156, 310–314. https://doi.org/10.1016/j.commatsci.2018.10.006.

Florea, M.V.A., Brouwers, H.J.H., 2013. Properties of various size fractions of crushed concrete related to process conditions and re-use. Cement Concr. Res. 52, 11–21. https://doi.org/10.1016/j.cemconres.2013.05.005.

Grangeon, S., Claret, F., Lerouge, C., Warmont, F., Sato, T., Anraku, S., Numako, C., Linard, Y., Lanson, B., 2013. On the nature of structural disorder in calcium silicate hydrates with a calcium/silicon ratio similar to tobermorite. Cement Concr. Res. 52, 31–37. https://doi.org/10.1016/j.cemconres.2013.05.007.

Gugin, N.Y., Yusenko, K.V., King, A., Meyer, K., Al-Sabbagh, D., Villajos, J.A., Emmerling, F., 2024. Lighting up industrial mechanochemistry: real-time in situ monitoring of reactive extrusion using energy-dispersive X-ray diffraction. Chem 10 (11), 3459–3473. https://doi.org/10.1016/j.chempr.2024.07.033.

Guo, H., Shi, C., Guan, X., Zhu, J., Ding, Y., Ling, T.C., Zhang, H., Wang, Y., 2018. Durability of recycled aggregate concrete – a review. Cement Concr. Compos. 89, 251–259. https://doi.org/10.1016/j.cemconcomp.2018.03.008.

Hu, Y., Li, J., Gao, P., Zhan, B., Yu, Y., Yang, Y., Hong, L., Yu, Q., 2024. Quantification of the residual mortar's distribution and wrapping degree in recycled concrete aggregate based on 3-D reconstruction technology. Constr. Build. Mater. 414. https://doi.org/10.1016/j.conbuildmat.2024.134983.

Jansen, D., Naber, C., Ectors, D., Lu, Z., Kong, X.M., Goetz-Neunhoeffer, F., Neubauer, J., 2018. The early hydration of OPC investigated by in-situ XRD, heat flow calorimetry, pore water analysis and 1H NMR: learning about adsorbed ions from a complete mass balance approach. Cement Concr. Res. 109, 230–242. https://doi.org/10.1016/j.cemconres.2018.04.017.

Karlsson, I., Rootzén, J., Johnsson, F., Erlandsson, M., 2021. Achieving net-zero carbon emissions in construction supply chains – a multidimensional analysis of residential building systems. Develop. Built Environ. 8. https://doi.org/10.1016/j.dibe.2021.100059.

Kim, J., 2022. Influence of quality of recycled aggregates on the mechanical properties of recycled aggregate concretes: an overview. Constr. Build. Mater. 328. https://doi.org/10.1016/j.conbuildmat.2022.127071. Elsevier Ltd.
Kim, H., Yoon, J., 2024. Automated mineral identification of pozzolanic materials using XRD patterns. J. Mater. Civ. Eng. 36 (12). https://doi.org/10.1061/JMCEE7.MTENG-17973.
Kumar Mehta, P., Monteiro, P.J.M., 2006. Concrete Microstructure, Properties, and Materials, third ed. McGraw-Hill Companies. https://doi.org/10.1036/0071462899.
Lal Chauhan, B., Jail Singh, G., 2023. Sustainable development of recycled concrete aggregate through optimized acid-mechanical treatment: a simplified approach. Constr. Build. Mater. 399, 132559. https://doi.org/10.1016/j.conbuildmat.2023.132559.
Le, H.B., Bui, Q.B., 2020. Recycled aggregate concretes – a state-of-the-art from the microstructure to the structural performance. Constr. Build. Mater. 257. https://doi.org/10.1016/j.conbuildmat.2020.119522. Elsevier Ltd.
Le Saoût, G., Kocaba, V., Scrivener, K., 2011. Application of the rietveld method to the analysis of anhydrous cement. Cement Concr. Res. 41 (2), 133–148. https://doi.org/10.1016/j.cemconres.2010.10.003. Elsevier Ltd.
Li, X., Scrivener, K.L., 2025. Quantification of nano-crystalline C-S-H in hydrated tricalcium silicate, Portland cement and fly ash cement using PONKCS method. Cement Concr. Res. 191, 107837. https://doi.org/10.1016/j.cemconres.2025.107837.
Li, B., Hou, S., Duan, Z., Li, L., Guo, W., 2021. Rheological behavior and compressive strength of concrete made with recycled fine aggregate of different size range. Constr. Build. Mater. 268. https://doi.org/10.1016/j.conbuildmat.2020.121172.
Li, J., Zhao, X., Yong, Q., Liang, J., Wu, H., 2023. Revealing the implicit and explicit attitudes of the public towards recycled aggregate based on psychological experiment. Develop. Built Environ. 16. https://doi.org/10.1016/j.dibe.2023.100280.
Liu, J.-C., Hossain, Md U., Xuan, D., Ali, H.A., Ng, S.T., Ye, H., 2023. Mechanical and durability performance of sustainable concretes containing conventional and emerging supplementary cementitious materials. Develop. Built Environ. 15, 100197. https://doi.org/10.1016/j.dibe.2023.100197.
Liu, Q., Cheng, A., Sun, C., Chen, K., Wang, Y., Li, W., 2024. Effects of aggregate's type and orientation on stress concentration and crack propagation of modeled concrete applied a shear force. J. Build. Eng. 95. https://doi.org/10.1016/j.jobe.2024.110340.
Lu, C., Yu, Q., Wei, J., Niu, Y., Zhang, Y., Lin, C., Chen, P., Shi, C., Yang, P., 2024. Influence of interface transition zones (ITZ) and pore structure on the compressive strength of recycled aggregate concrete. Constr. Build. Mater. 456. https://doi.org/10.1016/j.conbuildmat.2024.139299.
Martín-Morales, M., Zamorano, M., Valverde-Palacios, I., Cuenca-Moyano, G.M., Sánchez-Roldán, Z., 2013. Quality control of recycled aggregates (RAs) from construction and demolition waste (CDW). In: Handbook of Recycled Concrete and Demolition Waste. Elsevier Inc, pp. 270–303. https://doi.org/10.1533/9780857096906.2.270.
Mazhoud, B., Sedran, T., Cazacliu, B., Cothenet, A., Torrenti, J.M., 2022. Influence of residual mortar volume on the properties of recycled concrete aggregates. J. Build. Eng. 57. https://doi.org/10.1016/j.jobe.2022.104945.
Meier, R., Anderson, J., Verryn, S., 2012. Industrial X-ray diffraction analysis of building materials. Rev. Mineral. Geochem. 74 (1), 147–165. https://doi.org/10.2138/rmg.2012.74.4.
Mesecke, K., Warr, L.N., Malorny, W., 2022. Structure modeling and quantitative X-ray diffraction of C-(A)-S-H. J. Appl. Crystallogr. 55, 133–143. https://doi.org/10.1107/S1600576721012668.
Mumme, W.G., Hill, R.J., Bushnell-wye, G., Segnit, E.R., 1995. Rietveld crystal structure refinements, crystal chemistry and calculated powder diffraction data for the polymorphs of dicalcium silicate and related phases. https://api.semanticscholar.org/CorpusID:135973945.
Nilimaa, J., 2023. Smart materials and technologies for sustainable concrete construction. Develop. Built Environ. 15. https://doi.org/10.1016/j.dibe.2023.100177.
Nonat, A., 2004. The structure and stoichiometry of C-S-H. Cement Concr. Res. 34 (9), 1521–1528. https://doi.org/10.1016/j.cemconres.2004.04.035.
Otsu, N., 1979. A threshold selection method from gray-level histograms. IEIEE Transac. Sys. Man Cybernetic. 9 (1), 62–66.
O'Flynn, D., Reid, C.B., Christodoulou, C., Wilson, M.D., Veale, M.C., Seller, P., Hills, D., Desai, H., Wong, B., Speller, R., 2013. Explosive detection using pixellated X-ray diffraction (PixD). J. Instrum. 8 (3), P03007. https://doi.org/10.1088/1748-0221/8/03/P03007.
Pepe, M., Toledo Filho, R.D., Koenders, E.A.B., Martinelli, E., 2014. Alternative processing procedures for recycled aggregates in structural concrete. Constr. Build. Mater. 69, 124–132. https://doi.org/10.1016/j.conbuildmat.2014.06.084.
Piccinali, A., Diotti, A., Plizzari, G., Sorlini, S., 2022. Impact of recycled aggregate on the mechanical and environmental properties of concrete: a review. Materials 15 (5). https://doi.org/10.3390/ma15051818. MDPI.
Poon, C.S., Shui, Z.H., Lam, L., 2004. Effect of microstructure of ITZ on compressive strength of concrete prepared with recycled aggregates. Constr. Build. Mater. 18 (6), 461–468. https://doi.org/10.1016/j.conbuildmat.2004.03.005.
Rangel, C.S., Toledo Filho, R.D., Amario, M., Pepe, M., de Castro Polisseni, G., Puente de Andrade, G., 2019. Generalized quality control parameter for heterogenous recycled concrete aggregates: a pilot scale case study. J. Clean. Prod. 208, 589–601. https://doi.org/10.1016/j.jclepro.2018.10.110.
Ren, X., Tang, C., Xie, Y., Long, G., Ma, G., Wang, H., Tang, Z., 2024. 3D mesoscale study on the effect of ITZ and aggregate properties on the fracture behaviors of concrete based on discrete element method. J. Build. Eng. 83. https://doi.org/10.1016/j.jobe.2024.108450.
Renaudin, G., Francois, M., Evrard, O., 1999. Order and disorder in the lamellar hydrated tetracalcium monocarboaluminate compound. Cement Concr. Res. 29 (1), 63–69. https://doi.org/10.1016/S0008-8846(98)00184-7.
Sáez del Bosque, I.F., Zhu, W., Howind, T., Matías, A., Sánchez de Rojas, M.I., Medina, C., 2017. Properties of interfacial transition zones (ITZs) in concrete containing recycled mixed aggregate. Cement Concr. Compos. 81, 25–34. https://doi.org/10.1016/j.cemconcomp.2017.04.011.
Schneider, C.A., Rasband, W.S., Eliceiri, K.W., 2012. NIH image to ImageJ: 25 years of image analysis. Nat. Methods 9 (7), 671–675. https://doi.org/10.1038/nmeth.2089.
Seo, D.S., Choi, H.B., 2014. Effects of the old cement mortar attached to the recycled aggregate surface on the bond characteristics between aggregate and cement mortar. Constr. Build. Mater. 59, 72–77. https://doi.org/10.1016/j.conbuildmat.2014.02.047.
Su, Y., Xu, Y., Bao, Z., Ng, S.T., Gao, Q., 2024. Stakeholder interactions of government intervention in construction and demolition waste recycling market: a game theory approach. Develop. Built Environ. 18. https://doi.org/10.1016/j.dibe.2024.100391.
Tam, V.W.Y., Soomro, M., Evangelista, A.C.J., 2021. Quality improvement of recycled concrete aggregate by removal of residual mortar: a comprehensive review of approaches adopted. Constr. Build. Mater. 288. https://doi.org/10.1016/j.conbuildmat.2021.123066. Elsevier Ltd.
Teychenne, D.C., Franklin, R.E., Erntroy, H.C., Building Research Establishment, 1997. Design of Normal Concrete Mixes. Building Research Establishment.
Ulsen, C., Contessotto, R., dos Santos Macedo, R., Kahn, H., 2022. Quantification of the cement paste and phase's association in fine recycled aggregates by SEM-based image analysis. Constr. Build. Mater. 320. https://doi.org/10.1016/j.conbuildmat.2021.126206.
Vargas, P., Restrepo-Baena, O., Tobón, J.I., 2017. Microstructural analysis of interfacial transition zone (ITZ) and its impact on the compressive strength of lightweight concretes. Constr. Build. Mater. 137, 381–389. https://doi.org/10.1016/j.conbuildmat.2017.01.101.
Verian, K.P., Ashraf, W., Cao, Y., 2018. Properties of recycled concrete aggregate and their influence in new concrete production. Resour. Conserv. Recycl. 133, 30–49. https://doi.org/10.1016/j.resconrec.2018.02.005. Elsevier B.V.
Wang, R., Yu, N., Li, Y., 2020. Methods for improving the microstructure of recycled concrete aggregate: a review. Constr. Build. Mater. 242. https://doi.org/10.1016/j.conbuildmat.2020.118164. Elsevier Ltd.
Wang, B., Yan, L., Fu, Q., Kasal, B., 2021a. A comprehensive review on recycled aggregate and recycled aggregate concrete. Resour. Conserv. Recycl. 171. https://doi.org/10.1016/j.resconrec.2021.105565. Elsevier B.V.
Wang, Y., Liu, J., Zhu, P., Liu, H., Wu, C., Zhao, J., 2021b. Investigation of adhered mortar content on recycled aggregate using image analysis method. J. Mater. Civ. Eng. 33 (9). https://doi.org/10.1061/(asce)mt.1943-5533.0003864.
Xiong, Q., Baychev, T.G., Jivkov, A.P., 2016. Review of pore network modelling of porous media: experimental characterisations, network constructions and applications to reactive transport. J. Contam. Hydrol. 192, 101–117. https://doi.org/10.1016/j.jconhyd.2016.07.002. Elsevier B.V.
Yio, M.H.N., Wong, H.S., Buenfeld, N.R., 2017. Representative elementary volume (REV) of cementitious materials from three-dimensional pore structure analysis. Cement Concr. Res. 102, 187–202. https://doi.org/10.1016/j.cemconres.2017.09.012.
Zandomeneghi, D., Voltolini, M., Mancini, L., Brun, F., Dreossi, D., Polacci, M., 2010. Quantitative analysis of X-ray microtomography images of geomaterials: application to volcanic rocks. Geosphere 6 (6), 793–804. https://doi.org/10.1130/GES00561.1.
Zhan, B.J., Xuan, D.X., Poon, C.S., Scrivener, K.L., 2020. Characterization of interfacial transition zone in concrete prepared with carbonated modeled recycled concrete aggregates. Cement Concr. Res. 136. https://doi.org/10.1016/j.cemconres.2020.106175.
Zhang, J., Shi, C., Li, Y., Pan, X., Poon, C.S., Xie, Z., 2015. Influence of carbonated recycled concrete aggregate on properties of cement mortar. Constr. Build. Mater. 98, 1–7. https://doi.org/10.1016/j.conbuildmat.2015.08.087.
Zhang, C., Hu, M., Yang, X., Miranda-Xicotencatl, B., Sprecher, B., Di Maio, F., Zhong, X., Tukker, A., 2020. Upgrading construction and demolition waste management from downcycling to recycling in the Netherlands. J. Clean. Prod. 266. https://doi.org/10.1016/j.jclepro.2020.121718.
Zhao, Z., Remond, S., Damidot, D., Xu, W., 2013. Influence of hardened cement paste content on the water absorption of fine recycled concrete aggregates. Journal of Sustainable Cement-Based Materials 2 (3–4), 186–203. https://doi.org/10.1080/21650373.2013.812942.